一般セッション(口頭講演) | 4 JSAP-Optica Joint Symposia 2024：4.2 Photonics Devices, Photonic Integrated Circuit and Silicon Photonics

2024年9月17日(火) 14:45 ~ 18:15 A25 (朱鷺メッセ2F)

[17p-A25-2~11] 4.2 Photonics Devices, Photonic Integrated Circuit and Silicon Photonics

近藤 圭祐(宇都宮大)、 井上 尚子(住友電工)

英語発表
14:45 ~ 15:15
[17p-A25-2]
[JSAP-Optica Joint Symposia Invited Talk] Integrated photonics for quantum computation
○Nobuyuki Matsuda[1] (1.Tohoku Univ.)

英語発表
15:15 ~ 15:30
[17p-A25-3]
Performant Thin-Film Lithium Niobate Polarizer with an S-bend waveguide
○(M2)Fengyang Jin[1,3], Tingting Lang[2], Xiaowei Guan[3] (1.China Jiliang Univ., 2.ZJ Sci.&Tech Univ., 3.Jiaxing Inst. ZJU)

英語発表
15:30 ~ 15:45
[17p-A25-4]
Modelling of CO_2 Gas Sensing using Spectral Envelope of SoI Integrated Racetrack Resonator
○(DC)Shalini Vardhan[1], Naveen Kumar Gupta[2], Aditya Kushwaha[1], Priyanka Verma[1], Ritu Raj Singh[1] (1.Netaji Subhas University of Technology, Dwarka, Sector-3, Delhi-110078, India, 2.Indian Institute of Information Technology, Ranchi- 831014, India)

英語発表
15:45 ~ 16:00
[17p-A25-5]
Analysis of Ring Radius and Q-Factor for Enhanced Bandpass Filter performance in Racetrack Ring Resonators
○(DC)Shalini Vardhan[2], Naveen Kumar Gupta[1], Ritu Raj Singh[2] (1.IIIT Ranchi- 831014, India, 2.NSUT, Delhi-110078, India)

英語発表
16:00 ~ 16:30
[17p-A25-6]
[JSAP-Optica Joint Symposia Invited Talk] Diffraction-based on-chip optical neural network with high computational density
○Wencan Liu[1], Yuyao Huang[1], Run Sun[1], Tingzhao Fu[2], Hongwei Chen[1] (1.Tsinghua Univ., 2.National Univ. of Defense Technology)

英語発表
16:45 ~ 17:15
[17p-A25-7]
[JSAP-Optica Joint Symposia Invited Talk] Two-Dimensional Broadband Silicon Optical Beam Scanning Device for Free-Space Optical Communication

○Yuki Atsumi[1], Tomoya Yoshida[1], Ryosuke Matsumoto[1], Ryotaro Konoike[1], Kazuhiro Ikeda[1], Takashi Inoue[1], Keijiro Suzuki[1] (1.AIST)

🏷 奨励賞エントリー 🏷 英語発表
17:15 ~ 17:30
[17p-A25-8]
Cascading meta-devices for advanced functions and applications

○Jingcheng Zhang[1], Din Ping Tsai[1] (1.CityU)

🏷 英語発表
17:30 ~ 17:45
[17p-A25-9]
On-Chip Terahertz Polarization Control Enabled by Effective Medium

○(P)Weijie Gao[1], Withawat Withayachumnankul[2], Masayuki Fujita[1] (1.Osaka Univ., 2.Univ. Adelaide)

🏷 英語発表
17:45 ~ 18:00
[17p-A25-10]
Multiband Frequency-Tunable Millimeter-Wave Absorber

A. Shahzad[1], S. Ahmed[1], Q. A. Naqvi[1], ○Pankaj Kumar Choudhury[2] (1.Quaid-i-Azam Univ., 2.Zhejiang University)

🏷 英語発表
18:00 ~ 18:15
[17p-A25-11]
Mode Switching in Few-Mode Fibers Using Electric Field Controlled Dynamic Offset Coupling

○(D)Isha Sharma[1], Partha Roy Chaudhuri[1] (1.IIT Kharagpur)

Performant Thin-Film Lithium Niobate Polarizer with an S-bend waveguide

Fengyang Jin[1,3], Tingting Lang[2] and Xiaowei Guan[3]

[1] College of Optical and Electronic Technology, China Jiliang University, Hangzhou 310018, China, [2] School of Information and Electronic Engineering, Zhejiang University of Science and Technology, Hangzhou 310023, China, [3] Jiaxing Research Institute, Zhejiang University Jiaxing Key Laboratory of Photonic Sensing & Intelligent Imaging, Intelligent Optics and Photonics Research Center, Jiaxing Research Institute, Zhejiang University, Jiaxing 314000, China
E-mail: guanxw@zju.edu.cn

1. Introduction

Thin-film lithium niobate (TFLN) is currently emerging as a popular photonic integration circuit (PIC) platform for its versatile material superiorities[1]. Diverse performant devices have been demonstrated in the TFLN PICs, such as modulators[2] and passive devices[3]. While polarizer is a fundamental building block for the PICs, it is not a trivial to realize it in the TFLN PICs attributed to the birefringence of the material (X-cut TFLN) and the temporarily unavoidable slant sidewalls of the TFLN waveguide. TFLN waveguide polarizers have been experimentally realized using long period gratings[4] or Eule bends[5] showing extinction ratios (ERs) of ~ 20 dB and losses of ~ 1.5 dB. In this work, we demonstrate TFLN polarizers using an S-bend waveguide where TM modes are leaked out, exhibiting ERs ~ 50 dB and losses ~ 0.4 dB.

2. Design and measurement

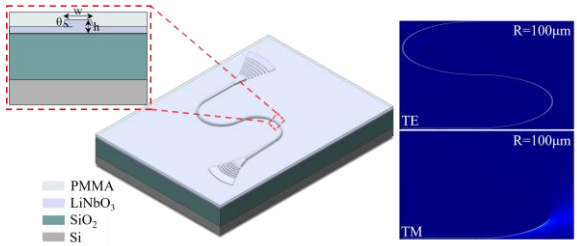

Fig. 2. 3D schematic of the proposed TFLN polarizer using an S-bend waveguide. Insets are for light propagations.

illustrates the structure of the proposed TFLN polarizer, where the commonly used ridge TFLN waveguide is employed with both the slab and ridge parts being 150 nm thick. The waveguide is initially tapered down from a 1.5-μm width to a 0.6-μm width and then successively connected to two 180° bend waveguides. As the transverse-magnetic (TM) mode is weakly confined in the 0.6-μm-wide TFLN waveguide, it is easily leaked out to the silica substrate and the PMMA cladding. However, the transverse-electric (TE) mode can transmit through the S-bend waveguide with low loss. By adjusting the widths and the bending radii of the S-bend waveguide, it is possible to achieve TE-pass polarizers with large ERs and low losses.

As depicted in Fig. 2, FDTD simulations suggest that with a sufficiently large bending radius (e.g., >40 μm), the polarizer's TE mode loss can be negligible. Conversely, the TM mode experiences increasing loss with larger bending

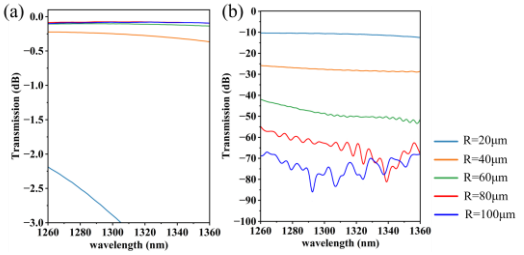

Fig. 1. Simulated transmissions for the TFLN polarizers with an S-bend waveguide. (a) TE mode. (b) TM mode.

radii, as even at 100 μm, the S-bend waveguide weakly confines light, and the total loss depends primarily on the S-bend waveguide's total length. Fabricated polarizers were measured using an O-band laser, with grating couplers as the interface with the fiber. The results, shown in Fig. 3, generally align with the simulations. For a polarizer with a 100-μm S-bend waveguide radius, the ERs exceed 50.6 dB and insertion losses are below 0.4 dB around a 1310 nm wavelength. Fabrication uniformity issues between the grating couplers for the polarizers and the straight waveguides for normalization posed some challenges. Extracting the bandwidth in terms of insertion loss was not straightforward. Nonetheless, the ERs generally exceed 30 dB for wavelengths from 1260 nm to 1340 nm.

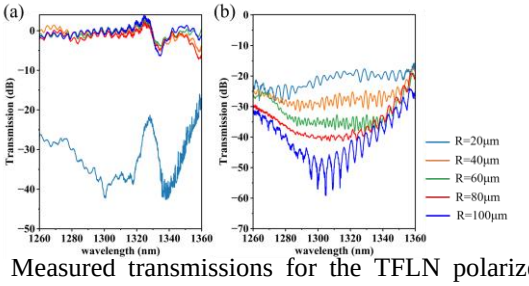

Fig. 3. Measured transmissions for the TFLN polarizers with an S-bend waveguide. (a) TE mode. (b) TM mode.

3. Conclusion

In conclusion, polarizers using an S-bend waveguide have been demonstrated for TFLN photonic circuits. The outstanding performances will potentially benefit many applications where pure polarization is required.

References

[1] Boes A, et al. Science. **379** (2023) 6627.
[2] Wang C, et al. Nature, **562** (2018) 7725.
[3] He J, et al. Opt. Express, **30** (2022) 19.
[4] Wei Jin, et al. Optica. **8** (2021) 1624.
[5] Weixi Liu, et al. Opt. Lett. **49** (2024) 2337.

Modelling of CO_2 Gas Sensing using Spectral Envelope of SoI Integrated Racetrack Resonator

Shalini Vardhan[1], Naveen Kumar Gupta[2], Aditya Kushwaha[1], Priyanka Verma[1], Ritu Raj Singh[1]
[1]Department of Electronics and Communication Engineering, Netaji Subhas University of Technology, Delhi, India
[2]Department of Electronics and Communication Engineering, Indian Institute of Information Technology, Ranchi, India
E-mail: shalini.vardhan.phd21@nsut.ac.in

1. Introduction

Silicon on Insulator (SoI) technology has tantalized the photonics world in terms of integrated device modeling encountering with numerous applications. Many gas sensors can be designed using SoI technique with lower scaling factor and higher operational speed [1]. The emission of Carbon dioxide is a natural process but excess emisson is a result of burning of fossil fuels, deforestation, increase in the use of automobiles [2]. People who work in automobile industries more likely face the respiratory problems, dizziness etc. To address these issues a gas sensor is designed to detect the excess of emitted CO_2. In this manuscript an approach to sense CO_2 gas using microring racetrack resonator is demonstrated. The sensing analysis is done on the basis of change in the refractive index (RI) in the cavity region which will result in the envelope spectrum shift.

2. Structure and Sensing Methodology

The 3D schematic for CO_2 sensing is represented by Fig 1, where P_{in} is used to inject optical power and P_{out} is used for the transmittance spectrum. The materials used in the design of optical ractetrack resonator are silicon (Si) as guiding material, silicon dioxide (SiO_2) as substrate and cladding as a gas chamber. The refractive index of Si and SiO_2 is calculated using Sellmeier's equation [3]. The RI of CO_2 is 1.489 [4]. The width and height of Si is represented by x and y axis as shown Fig 1, which are 400 nm and 220 nm [5], [6]. For ease of simulation the coupling gap between straight waveguide and racetrack waveguide is 100 nm, the ring radius is 5 µm and the coupling setion inserted between the splitted ring is of 9.7 µm. The operational wavelength range is from 1350 nm to 1850 nm.

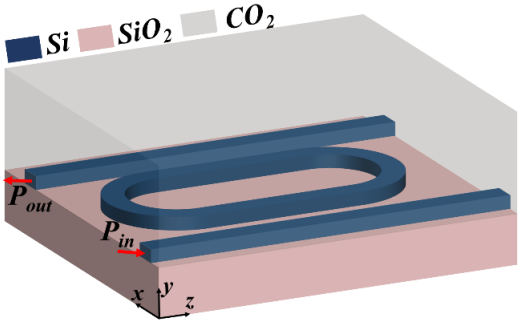

Figure 1. 3D schematic of Micro Racetrack Resonator for CO_2 gas sensing

For CO_2 sensing a gaseous chamber of glass is made for the concentration of air volume fraction. When the ppm in the gaseous chamber exceeds (concentration of CO_2 gas), the envelope spectrum of the optical racetrcak resonator shifts from the referenced envelope spectrum. The RI of different percentage by volume of CO_2 – air mixture is obtained by Lorentz-Lorenz mixing rule [7].

3. Result and Discussion

The output obtained from the optical racetrack resonator is shown in Fig 2 expressed in the form of power transmittance. The envelope spectrum for SiO_2 and CO_2 gas sensor shows the shift in the wavelength. To get the shifted spectrum, the refractive index of CO_2 gas is replaced with SiO_2, in the clading region of the racetrack waveguide. The sensor envelope spectrum shows the shift of 29.21 nm from the reference envelope spectrum. The sensitivity of the gas sensor is the fraction of change in resonanace wavelength by the change in the refractive index expressed in nm/RIU mentioned in equation 1.

$$S = \frac{\Delta\lambda_c}{\Delta n}\ nm/RIU \qquad (1)$$

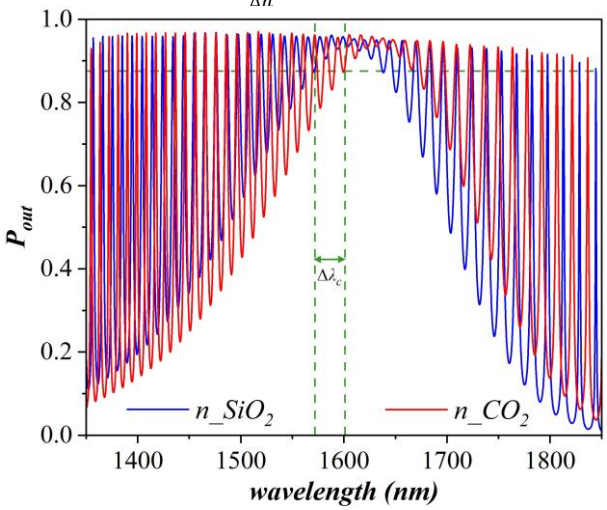

Figure 2. Envelope Spectrum for CO_2 gas sensor referenced with the silica glass cladding

4. Conclusion

A gas sensor is designed using optical racetrack resonator for 1350 nm to 1850 nm wavelength range. The practical application of CO_2 gas sensor is utilized at the industrial places where carbon emission poses the risk for the human health. The sensitivity obtained is 595.88 nm/RIU with a shift of 29.21 nm.

REFERENCES

[1] C. Ranacher *et al.*, "Characterization of Evanescent Field Gas Sensor Structures Based on Silicon Photonics," *IEEE Photonics J.*, vol. 10, no. 5, pp. 1–14, Oct. 2018, doi: 10.1109/JPHOT.2018.2866628.
[2] R. Waheed, D. Chang, S. Sarwar, and W. Chen, "Forest, agriculture, renewable energy, and CO2 emission," *J. Clean. Prod.*, vol. 172, pp. 4231–4238, Jan. 2018, doi: 10.1016/j.jclepro.2017.10.287.
[3] S. Vardhan and R. R. Singh, "Design, simulation and performance comparison of SoI rectangular waveguide and SMF for methane detection," in *Integrated Photonics Platforms II*, May 2022, p. 32, doi: 10.1117/12.2621459.
[4] C. Jesus Gouveia, A. Markovics, J. M. Baptista, B. Kovács, and P. A. S. Jorge, "Colorimetric and refractometric measurements of carbon dioxide," May 2011, p. 80013C, doi: 10.1117/12.892091.
[5] S. Vardhan and R. R. Singh, "Optimization and Comparative Analysis of Rectangular and Slot Waveguide based Symmetric Ring and Racetrack Resonators for SoI Photonic Integrated Filters," *Silicon*, no. 0123456789, 2024, doi: 10.1007/s12633-024-02879-z.
[6] S. Vardhan and R. R. Singh, "Poynting Vector Analysis of SoI based Hybrid Plasmonic Rectangular Waveguide," in *JSAP-Optica Joint Symposia 2022 Abstracts*, 2022, p. 20p_C304_13, [Online]. Available: https://opg.optica.org/abstract.cfm?URI=JSAPO-2022-20p_C304_13.
[7] R. R. Singh, N. Malviya, and V. Priye, "Parametric Analysis of Silicon Nanowire Optical Rectangular Waveguide Sensor," *IEEE Photonics Technol. Lett.*, vol. 28, no. 24, pp. 2889–2892, Dec. 2016, doi: 10.1109/LPT.2016.2624501.

Analysis of Ring Radius and Q-Factor for Enhanced Bandpass Filter performance in Racetrack Ring Resonators

Naveen Kumar Gupta[1], Shalini Vardhan[2], Ritu Raj Singh[2]
[1]Department of Electronics and Communication Engineering, Indian Institute of Information Technology, Ranchi, India
[2]Department of Electronics and Communication Engineering, Netaji Subhas University of Technology, Delhi, India
E-mail: naveenkumaar.ece@gmail.com

1. Introduction

There have been various studies on the racetrack ring resonators, which aimed to calculate various resonators parameters, Free Spectral Range (FSR), Full Width at Half Maximum (FWHM), Finesse (F), Quality (Q) factor [1], and Sensitivity. Optical Resonators have numerous applications in Photonic Integrated Circuits (PIC), from Optical filters to Sensors [2], Switches [3], Lasers [4], Modulators [5], Multiplexers [6]. In this research article, an optical Racetrack Ring Resonator (RTRR) is proposed as a band pass filter and the effect of ring radius (R) is demonstrated to optimize the Q-factor for bandpass filter (BPF) applications. The wavelength band for the study of band pass filter ranges from 1300 nm to 1900 nm.

2. Structure and Methodology

The RTRR is based upon the Silicon on Insulator (SoI) technology, in which a racetrack structure of Silicon material (Si) is mounted over a dielectric substrate, silicon dioxide (SiO_2) as illustrated by Fig. 1. To design a RTRR, a ring of 'R' radius is splitted into two equal halves and a coupling section of 9.77 µm is inserted. For Quasi TE [7] wave propagation, RTRR uses two straight waveguides and a racetrack waveguide and the gap between them is 100 nm. To design such optical resonators, the dimensional sizes of silicon wafers uses the cross section of 400 nm×220 nm [8]. For the study of Q-factor, R is varied as 1 µm, 2 µm, 5 µm and 10 µm.

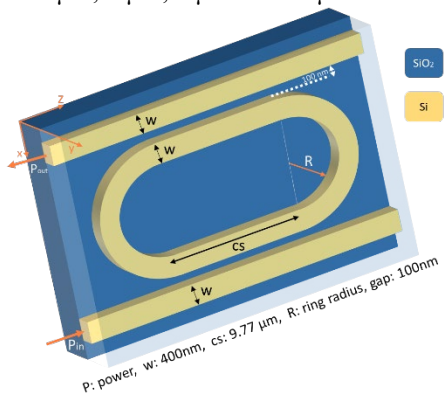

Fig. 1. 3D schematic of Racetrack Ring Resonator

Transverse Electric (TE) power propagates through the rectangular waveguide's input port P_{in}. The power injected through P_{in} gets coupled to the racetrack waveguide and circulates in it. Then power recouples to the upper straight waveguide and output is taken from P_{out} in the form of transmittance spectrum as shown in Fig. 2 and Fig. 3.

3. Result and Discussion

The RTRR with different R (1 µm, 2 µm, 5 µm and 10 µm) is analyzed using finite element method (FEM). The results shown in Fig. 3 illustrates that on increasing R values the envelope spectrum shifts, the number of resonance notch increases, and the spectrum becomes more compressed, which results in the decrease of FSR and FWHM along with the blue shift. To examine the impact of R, the Q-factor is computed in terms of central wavelength (λc) and FWHM, using the following formula.

$$Q = \frac{\lambda_C}{FWHM} \quad (1)$$

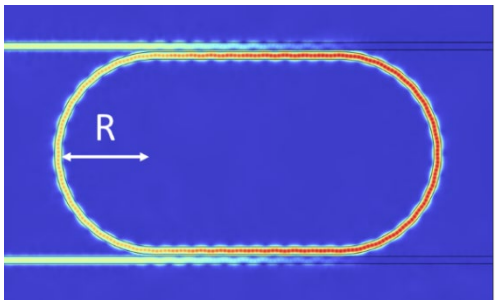

Fig. 2. Power propagation in RTRR

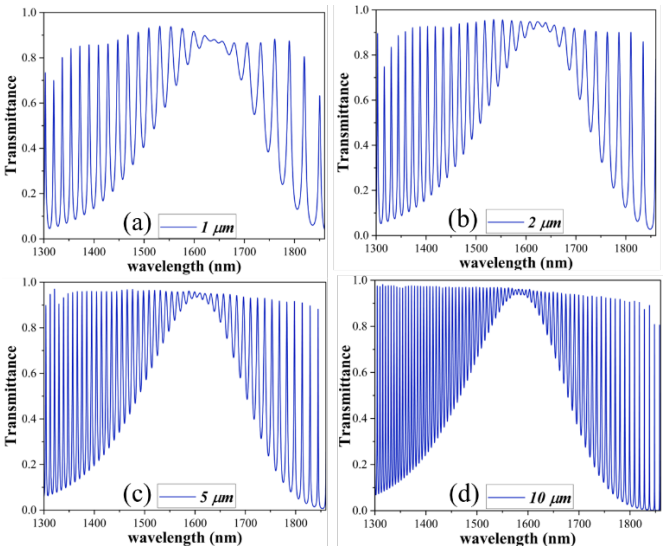

Fig. 3. Transmittance for R = (a) 1 µm; (b) 2 µm; (c) 5 µm; and (d) 10 µm

4. Conclusion

In this research work, the RTRR based filter has Q-factor of 7.304, 7.439, 7.616, 7.969 for R = 1 µm, 2 µm, 5 µm and 10 µm, respectively. The Q factor listed are not significantly varied on increasing R, but other dimensional parameters (i.e. '*cs*' and gap) may have considerable impact on Q-factor. Hence, the proposed RTRR can be significantly utilized as an BPF.

REFERENCES

[1] T. Sun, W. Niu, and M. Xia, "Racetrack microring resonator with improved quality factor based on asymmetric waveguide bend," *Opt. Commun.*, vol. 529, p. 129092, Feb. 2023, doi: 10.1016/j.optcom.2022.129092.
[2] Chung-Yen Chao and L. J. Guo, "Design and optimization of microring resonators in biochemical sensing applications," *J. Light. Technol.*, vol. 24, no. 3, pp. 1395–1402, Mar. 2006, doi: 10.1109/JLT.2005.863333.
[3] S. Gulde, A. Jebali, and N. Moll, "Optimization of ultrafast all-optical resonator switching," *Opt. Express*, vol. 13, no. 23, p. 9502, 2005, doi: 10.1364/OPEX.13.009502.
[4] X. Shen, H. Choi, D. Chen, W. Zhao, and A. M. Armani, "Raman laser from an optical resonator with a grafted single-molecule monolayer," *Nat. Photonics*, vol. 14, no. 2, pp. 95–101, Feb. 2020, doi: 10.1038/s41566-019-0563-7.
[5] Y. Amemiya, T. Tokunaga, Y. Tanushi, and S. Yokoyama, "Optical modulator using metal-oxide-semiconductor type Si ring resonator," *Opt. Rev.*, vol. 16, no. 3, pp. 247–251, May 2009, doi: 10.1007/s10043-009-0046-z.
[6] D. Wu, Y. Wu, Y. Wang, J. An, and X. Hu, "Four-channel optical add-drop multiplexer based on dual racetrack micro-ring resonators," *Opt. Commun.*, vol. 354, pp. 386–391, Nov. 2015, doi: 10.1016/j.optcom.2015.06.028.
[7] F. Dell'Olio, V. M. N. Passaro, G. Z. Mashanovich, and F. De Leonardis, "Micro-racetrack coupled-resonator optical waveguides in silicon photonic wires," *J. Opt. A Pure Appl. Opt.*, vol. 10, no. 6, p. 064003, Jun. 2008, doi: 10.1088/1464-4258/10/6/064003.
[8] S. Vardhan and R. R. Singh, "Optimization and Comparative Analysis of Rectangular and Slot Waveguide based Symmetric Ring and Racetrack Resonators for SoI Photonic Integrated Filters," *Silicon*, vol. 16, no. 7, pp. 2913–2926, May 2024, doi: 10.1007/s12633-024-02879-z.

Diffraction-based on-chip optical neural network with high computational density

○ Wencan Liu[1], Yuyao Huang[1], Run Sun[1], Tingzhao Fu[2] and Hongwei Chen[1]

Tsinghua University, China [1], National University of Defense Technology, China [2]

E-mail: chenhw@tsinghua.edu.cn

1. Introduction

The rapid advancement of artificial intelligence has led to substantial progress in various fields with deep neural networks (DNNs). However, complex tasks often require increasing power consumption and greater resources of electronics. On-chip optical neural networks (ONNs) are increasingly recognized for their power efficiency, wide bandwidth, and capability for light-speed parallel processing. In our previous work [1], we proposed on-chip diffractive optical neural networks (DONNs) to offer the potential to map a larger number of neurons and connections onto optics. To further improve the computational density and integration level, we proposed ultra-compact DONNs designed with the structure re-parameterization algorithm [2] and experimentally verified their performance [3], which increased the computational density by more than an order of magnitude.

2. Structure design and numerical modeling

The DONN chips developed consist of metalines, which represent the hidden layer of a neural network. These metalines consist of slots filled with SiO_2, serving as trainable parameters, optimized in the training process. To accurately model the propagation process in the metaline, slot groups and extra length between adjacent layers are utilized, resulting in the relatively large chip scale [1].

Given the challenges in directly modeling on-chip DONNs, particularly in accurately depicting the interaction between the silicon slots and the optical field, a deep complex neural network (DCNN) is employed to simulate the complex interactions in each metaline. Consequently, this approach allows for a precise numerical representation of the on-chip light propagation [2]. The architecture of the DONN with two hidden layers is illustrated in Fig. 1(a) and the modeling process is depicted in Fig. 1(b). The dimensions of the structure are set to 53 um in length and 30 um in width, with distance between adjacent layers set as 15 um. The input and output layers consist of four input straight waveguides and three output taper waveguides, respectively. As a proof of the design method, the chip was fabricated based on the SOI platform. The SEM images in Fig. 1(c) illustrates the on-chip DONN with 2 hidden layers and diffractive units. The experimental result of the chip revealing an accuracy of 93.3% in Iris plants dataset, aligning with numerical predictions [3].

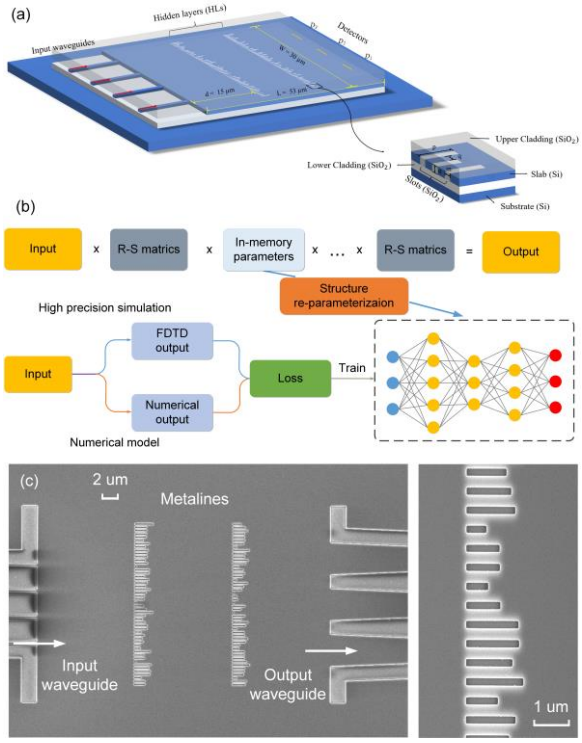

Fig. 1. (a) The architecture of the DONN. (b) Numerical modeling on structure re-parameterization algorithm. (c) SEM images of the DONN chip with 2 hidden layers and diffractive units.

3. Conclusions

In summary, DONN has significant advantage in mapping a large number of connections and trainable parameters on chip, allowing for passive computing on a compact structure. Furthermore, with utilization of the structure re-parameterization algorithm, we can greatly improve the parameter integration while achieving computational density of 18.6 POPS/mm^2.

Acknowledgements

This work was supported by the National Natural Science Foundation of China (62135009).

References

[1] T. Fu et al. “Photonic machine learning with on-chip diffractive optics,” Nat. Commun. 14, 70 (2023).

[2] W. Liu et al. “C-DONN: compact diffractive optical neural network with deep learning regression,” Opt. Express 31, 22127–22143 (2023).

[3] W. Liu et al. “Ultra-compact optical neural network chip,” CLEO 2024, no. SM4M. 5

Two-Dimensional Broadband Silicon Optical Beam Scanning Device for Free-Space Optical Communication

AIST [1], °Yuki Atsumi[1], Tomoya Yoshida[1], Ryosuke Matsumoto[1], Ryotaro Konoike[1], Kazuhiro Ikeda[1], Takashi Inoue[1], Keijiro Suzuki[1]

E-mail: y-atsumi@aist.go.jp

Silicon photonics-based beam scanning technology is expected to be introduced into short-distance free-space optical (FSO) communication applications such as inter/intra rack communications in data centers and indoor mobile communications in beyond-5G mobile communications [1]. In this report, we present our recent work about a broadband two-dimensional (2D) Si beam scanning device shown in Fig. 1 that integrates 128-port three-dimensionally-structured optical surface couplers known as “elephant couplers”[2-4]. This device can realize high-capacity FSO signal transmission by introducing wavelength-division multiplexing (WDM) technology. The fabricated device shows a fiber-to-fiber insertion loss of 5.6 dB and a 1-dB spectrum bandwidth of 40 nm. We obtained a beam scanning operation with the scannable beam-angle range and the resolution range of 5.3 deg × 2.5 deg and 0.35 deg × 0.36 deg, respectively, by introducing a commercial imaging lens. Using this system, we have demonstrated FSO transmission of a 10 Gbps non-return-to-zero on-off-keying signal successfully within a wavelength range from 1530 to 1590 nm with a fixed receiver position as shown in Fig. 2.

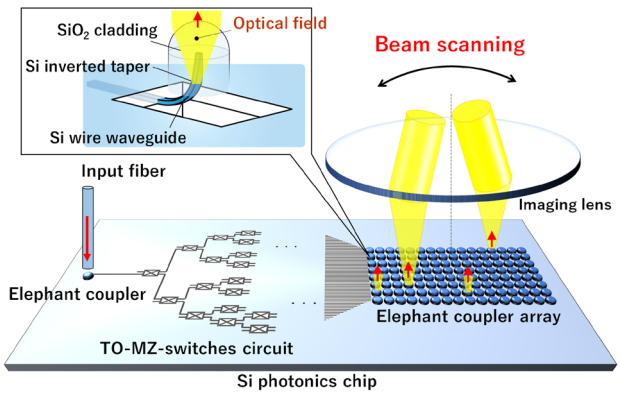

Fig. 1 Schematic images of silicon beam scanner.

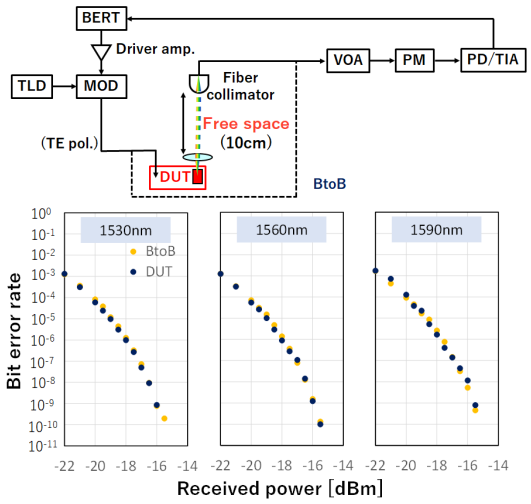

Fig. 2 FSO signal transmission

Acknowldgment

These research results were obtained from commissioned research conducted by the National Institute of Information and Communications Technology (NICT), Japan with the grant number of JPJ012368C08401.

References

[1] K. Wang, et al., J. Lightw. Technol., 37(2), pp. 619-626, 2019.
[2] T. Yoshida, et al., IEEE Photon. Technol. Lett., 32(20), pp. 1319-1322, 2020.
[3] Y. Atsumi, et al., Proc. Optical Fiber Communication Conf. (OFC), M3C.4, San Diego, CA, 2023.
[4] Y. Atsumi, et al., IEICE trans. Electron., E106-C(11), pp. 739-747, 2023.

Cascading meta-devices for advanced functions and applications

Jing Cheng Zhang[1] and Din Ping Tsai[1]

[1]Department of Electrical Engineering, City University of Hong Kong, Hong Kong SAR, CHINA
E-mail: jzhang2442-c@my.cityu.edu.hk

1. Introduction

Metasurfaces, recognized as subwavelength antenna collections, offer many possibilities for managing electromagnetic waves and streamlining the dimensions and intricacy of electromagnetic apparatus. These structures can govern diverse aspects of electromagnetic waves, encompassing amplitude, wavelength, polarization, phase, orbital angular momentum, and more. Multilayer meta-devices provide a greater degree of freedom to manipulate the light and have a better ability to perform various functions. In this thesis, various multilayer meta-devices have been systematically developed for advanced functions and applications, such as 6G communications, chiral imaging, and light field control for other advanced applications.

2. Methods and results

The polarization of light serves as a valuable information channel extensively explored in optical devices. We present an experimental demonstration of a chiral imaging meta-device featuring extensive area coverage and broadband chirality control, achieved through applying nanoimprint technology to create a centimeter-scale Moiré meta-device, as shown in Fig. 1(a) [1]. Tunable Airy beams with controllable propagation trajectories have garnered widespread interest in various fields. We present a novel method utilizing a dual metasurface system to overcome these limitations and significantly enhance the practical potential of the Airy beam, as shown in Fig. 1(b) [2]. Sixth-generation communication technology is currently undergoing active development, with expectations of surpassing its fifth-generation predecessor in speed and performance. To comprehensively govern the propagation direction and coverage area of terahertz beams, we have devised meta-devices featuring synthetic phase designs of rotary doublet Airy beams and triplet Gaussian beams with adjustable focal properties, as shown in Fig. 1(c) [3]. Our approach involves encoding a cubic phase profile and two off-axis Fresnel lens phase profiles across the two metasurfaces. Validation of the proposed strategy is achieved through simulation and experimental results. The proposed meta-device effectively addresses existing limitations and lays the foundation for expanding the applicability of Airy beams across diverse domains, including light-sheet microscopy, laser fabrication, optical tweezers, and beyond.

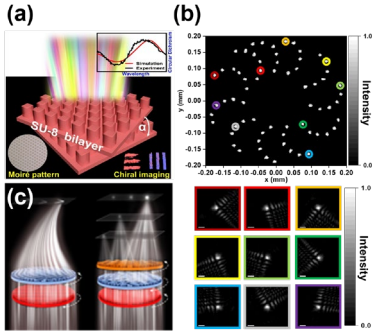

Fig. 1. (a) Chiral imaging meta-device, (b) Miniature tunable Airy beam optical meta-device, (c) A 6G meta-device for 3D varifocal

3. Conclusions

In summary, the exploration of metasurfaces and meta-devices in this thesis uncovers innovative possibilities, ranging from precise control over EM waves to communication, imaging, sensing, and beyond applications. The advancements presented hold significant promise for shaping the future of EM devices and technologies. To envision a broader perspective, metasurfaces exhibit numerous advantages over conventional devices, making them a promising avenue for developing new applications using established high-dimensional modulation principles.

Acknowledgements

This work is supported by the University Grants Committee / Research Grants Council of the Hong Kong Special Administrative Region, China [Project No. AoE/P-502/20, CRF Project: C1015-21E; C5031-22G, GRF Project: CityU15303521; CityU11305223; CityU11310522; CityU11300123, and Germany/Hong Kong Joint Research Scheme: G-CityU 101/22], City University of Hong Kong [Project No. 9380131, 9610628, and 7005867], and National Natural Science Foundation of China [Grant No. 62375232].

References

1. Zhang J C, et al. Miniature tunable Airy beam optical meta-device. Opto-Electronic Advances, 2024, 7(2): 230171-1-230171-8.
2. Zhang J C, et al. Nanoimprint meta-device for chiral imaging. Advanced Functional Materials, 2023, 33(49): 2306422.
3. Zhang J C, et al. A 6G meta-device for 3D varifocal. Science Advances, 2023, 9(4): eadf8478.

有効媒質によるオンチップテラヘルツ偏光制御

On-Chip Terahertz Polarization Control Enabled by Effective Medium

阪大基礎工 [1]，アデレード大 [2]，○Weijie Gao[1]，Withawat Withayachumnankul[2]，冨士田 誠之 [1]

Osaka Univ. [1], Univ. Adelaide [2] ○ Weijie Gao[1], Withawat Withayachumnankul[2], Masayuki Fujita[1]

E-mail: gao.weijie.es@osaka-u.ac.jp

We have proposed a solution for terahertz wave on-chip transmission [1], filtering [2], and polarization manipulation [3] with unprecedented performance based on the concept of effective medium [4]. The effective medium is realized by periodically perforating the silicon slab with a period in the deep subwavelength region. As a result, the effective medium can be treated as a homogenous material within the operation frequency range with a tailorable anisotropic permittivity tensor that is only mildly frequency dependent. The unique characteristics of the effective medium play a critical role in enhancing the performance of various terahertz integrated devices. In particular, the anisotropy of the effective medium can significantly increase the polarization extinction ratio (PER) for polarization beam splitters and rotators. This study mainly focuses on the impacts on PER of a terahertz integrated polarization rotator enabled by the effective medium.

As shown in Figs. 1(a)-(b), the proposed polarization rotator consists of two inversely symmetric tapered cores based on silicon and effective medium, respectively. In-plane effective medium claddings are introduced to surround the cores, where the effective medium can be realized by creating holes in the silicon slab in a hexagonal lattice, as shown in Fig. 1(c). Given a perforation period of 100 μm, the anisotropic relative permittivities can be obtained based on Maxwell-Garnett's effective medium theory [4], and they decrease with the hole diameter increasing, as shown in Fig. 1(d). Blind holes realize the effective medium core to rotate the optical axis, while the claddings are through holes. Here, the effective medium core is designed with an identical permittivity with that of the upper claddings realized with a hole diameter of 90 μm. With such a configuration, the input mode with the E_y polarization can be gradually rotated to its orthogonal counterpart after a sufficiently long conversion length based on the mode evolution theory. Notably, the lower cladding is introduced, which can vary the polarization states by changing its permittivity, leading to different PERs. As shown in Fig. 1(f), by gradually changing Δd, i.e., by reducing the hole size of the lower cladding, PER can be increased over the operation frequency range, where Δd is defined as the difference in diameter of holes between the upper and lower claddings. This is mainly due to the optical axis's varying rotation angle determined by the asymmetric claddings' birefringence. The proposed method promises terahertz on-chip polarization control like half-wave and quarter-wave plates for free-space waves.

This work was partly supported by JST CREST (JPMJCR21C4), the ARC Discovery Project (No. ARC DP220100489), and KAKENHI (24H00031).

参考文献

[1]. W. Gao *et al.*, *Optics Express*, **27**, 26 (2019).
[2]. W. Gao *et al.*, *APL Photonics*, **6**, 076105 (2021).
[3]. W. Gao *et al.*, *Proceedings of APMC*, 100 (2021).
[4]. A. V. Subashiev and S. Luryi, *Journal of Lightwave Technology*, **24**, 3(2006).

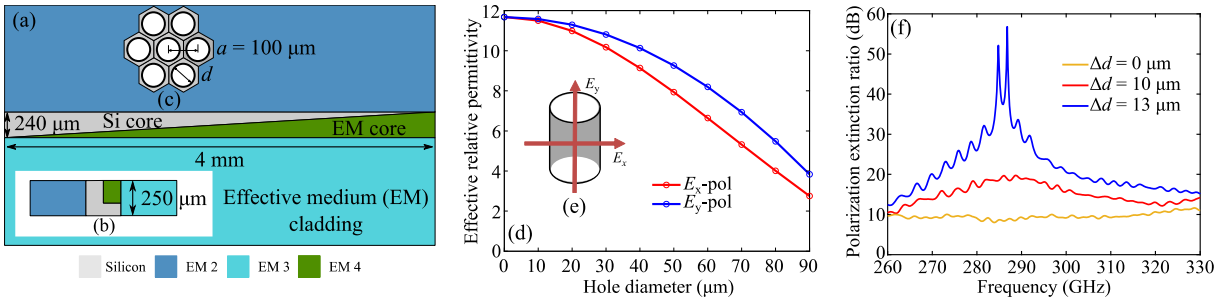

Fig.1. (a) Top view and (b) cross-section (center) view of terahertz integrated polarization rotator based on artificial homogeneous material. (c) Magnified view of the hexagonal lattice of the realized effective-medium cladding. (d) Effective relative permittivity as a function of the air hole diameter of the realized effective medium in (c). (e) 3D view of an air hole in silicon with an indication of polarization. (f) Polarization extinction ratio of the polarization rotator with different configurations of the asymmetric claddings.

Multiband Frequency-Tunable Millimeter-Wave Absorber

A. Shahzad[1, 2], S. Ahmed[1], Q. A. Naqvi[1], and Pankaj K. Choudhury[2*]

[1]Department of Electronics, Quaid-i-Azam University, Islamabad, 45320 Pakistan
[2]International Research Center for Advanced Photonics, Zhejiang University, Haining 314400, China
*E-mail: pkchoudhury@ieee.org

1. Introduction

The use of wireless electronic devices, such as sensors, radar detectors and cell phones, has resulted in a complex electromagnetic (EM) environment that causes significant EM pollution [1]. To avoid these, absorbers with effective EM attenuation are indispensable [1–3]. Within the context, functional materials and structures having adjustable or adaptive absorption characteristics are of paramount importance to efficiently absorb EM radiation in challenging circumstances [4–6]. Frequency-tunable absorbers are commonly employed in microwave frequency bands. Herein, we present a multiband millimeter-wave absorber comprising a multilayer hybrid structure of graphene-copper-FR4-copper to achieve multiband frequency-tunable millimeter-wave absorption. We emphasize on the theoretical framework, design methodology, and results based on simulations.

2. Device Modelling and Theory

Figure 1a illustrates the schematic of the absorber, which consists of a patterned graphene and copper layers, which are isolated by the PET dielectric medium. The structure is backed by a copper layer (of thickness slightly greater than the skin depth) acting as a reflective ground plane. Also, the FR4 dielectric substrate is placed between the patterned copper layer and the copper ground plane. We choose the unit cell size to be p = 2.5 mm (fig. 1a). Figure 1b depicts the cross-sectional side view of the structure. In the design, the patterned graphene and copper have the same period as the unit cell structure. Also, the side lengths and strip widths of the patterned graphene and copper are identical, with their respective values as l = 1.5 mm and w = 0.2 mm (fig. 1a).

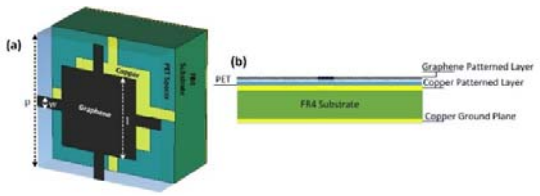

Fig. 1. Schematic of the multiband frequency tunable absorber; (a) top view, and (b) cross-sectional view.

We investigate the spectral properties using the finite integration technique implemented in the CST Microwave Studio platform. The spectral absorption characteristics are determined by

$$A(f) = 1 - |S_{11}|^2 - |S_{21}|^2. \quad (1)$$

Since copper as the ground plane makes almost vanishing transmission (i.e., $S_{21} \approx 0$), the absorptance will be

$$A(f) = 1 - |S_{11}|^2. \quad (2)$$

Thus, a single port network can be achieved with the input impedance

$$Z_{in} = Z_0(1 + S_{11})/(1 - S_{11}). \quad (3)$$

Z_{in} is solely determined by S_{11}, and as $S_{21} \approx 0$, the impedance matching condition, given by $[Re(Z_{in}) = Z_0 = 377\Omega, Im(Z_{in}) = 0]$, is achieved. This condition marks the point where the nearly perfect absorption occurs.

3. Results and Discussion

Figure 2 illustrates the plots of reflection coefficients S_{11} for different values of graphene surface impedance. The simulated results exhibit shifts in reflection minima in three subbands (75.5–81GHz, 88–93GHz, and 101.8–106.5GHz) within the W-band as the graphene surface impedance varies from 1000 Ω/Sq to 180 Ω/Sq. Notably, the reflection minima consistently remain less than −17 dB (corresponding to absorptance ≥98%). This is attributed to the impedance matching conditions met at different frequencies in the stated multiple frequency bands.

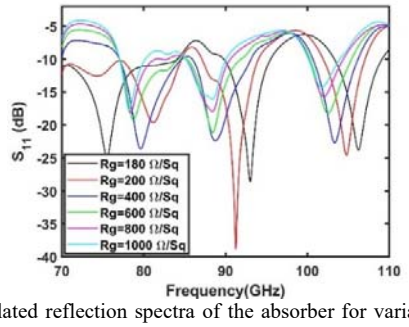

Fig. 2. Simulated reflection spectra of the absorber for variable graphene sheet impedance.

4. Conclusion

A multiband frequency-tunable millimeter-wave absorber comprising a patterned graphene-FR4-copper based hybrid structure has been studied, and the results yield tunability along with high absorption. The structure facilitates excellent frequency tunability range in three different bands, namely 75.5–81GHz, 88–93GHz, and 101.8–106.5GHz, within the W-band. It has been found that the millimeter wave absorber demonstrates over 98% absorptance throughout the frequency-tuning process.

Acknowledgement

PKC acknowledges the financial support by Zhejiang University (China) through the grant 1113000*194232301/002.

References

[1] E. F. Knott, J. F. Schaeffer, and M. T. Tulley, SciTech Publishing (2004).
[2] C. M. Watts, X. Liu, and W. J. Padilla, Adv. Mater. **24** (2012).
[3] S. Zhong and S. He, Sci. Rep. **3** (2013) 2083.
[4] M. A. Baqir and P. K. Choudhury, J. Opt. Soc. Am. B **36** (2019) F123.
[5] M. Pourmand, P. K. Choudhury, and M. A. Mohamed, Sci. Rep. **11** (2021) 3603.
[6] M. Pourmand and P. K. Choudhury, IEEE Trans. Nanotechnol. **21** (2022) 586.

Mode Switching in Few-Mode Fibers Using Electric Field Controlled Dynamic Offset Coupling

Isha Sharma[1], Partha Roy Chaudhuri[1*]
[1] Department of Physics, Indian Institute of Technology Kharagpur-721302, India
***email : roycp@phy.iitkgp.ac.in**

I. INTRODUCTION

In recent years, there has been a significant R&D focus on developing optical fiber-based technologies in photonics and broadband communication systems. The surge in data communication and cloud computing has led to an exponential increase in communication traffic. To address this challenge, few-mode fibers and mode division multiplexing (MDM) have become promising solutions. Mode converters are essential components in MDM systems, and various types have been proposed and experimentally validated. These converters utilize a range of techniques, including acousto-optic transducers and structured optical waveguides, to achieve their functionality [1].

We have developed an all-fiber setup designed for selectively exciting and switching between higher-order modes in a few-mode fiber. Previously, we introduced a novel method utilizing cantilever beam deflection techniques to detect surrounding electric fields. In this study, we apply the cantilever technique to achieve mode switching by introducing a controlled perturbation in the input launching conditions. The fiber is coated with $BiFe_{0.9}Co_{0.1}O_3$, serving as a probe sample, and is placed within an electric field for testing.

II. EXPERIMENTAL DETAILS AND RESULT

The light is coupled into one end of a single-mode fiber (SMF) from an input He-Ne laser source using a light coupling unit, shown in Fig. 1. The other end of the SMF is coated with our probe material (coated length 1.0 cm with coated thickness of 0.28 mm). A dual-mode fiber (DMF) is positioned directly in line with the exit of the input cantilever fiber, situated between two electric field plates. When an electric field is applied, the coated fiber deflects due to the induced polarization of the probe sample. This deflection modulates the input launching conditions, leading to changes in mode excitation within the fiber and resulting in the switching of the output mode.

Initially, light is coupled from SMF into the DMF through fiber-to-fiber transmission. This approach ensures close proximity between the fibers, establishing nearly ideal alignment to facilitate the excitation of the desired fundamental mode. Upon applying the electric field, we observe mode switching within the DMF. Figure 2 visually depicts the mode profiles and their transformations as the electric field intensity varies, specifically showing cases with different plate separations. In this scenario, we observe a transition from a circularly symmetric mode to an azimuthally asymmetric mode during the switching process.

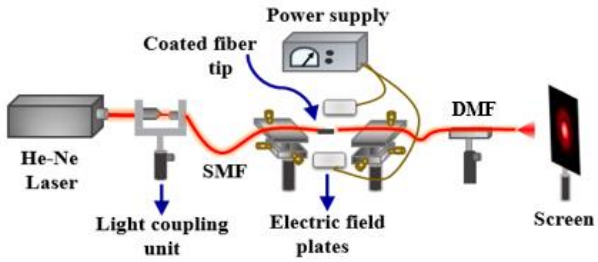

Fig. 1. Schematic of experimental set-up.

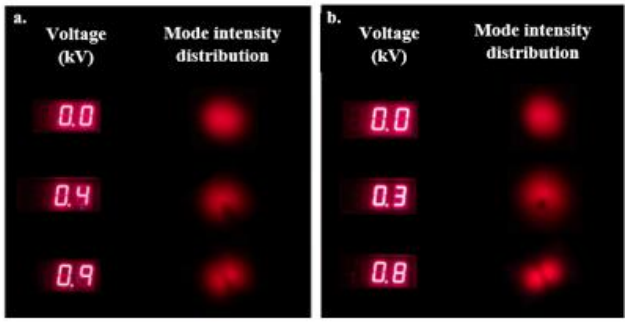

Fig.2. Real time monitoring of mode intensity distribution at different voltage values at fiber exit for varying plates distance at (a) 1.4 (b) 1.9 cm.

III. CONCLUSIONS

We demonstrate a novel method to perform an automated mode switching within a few-mode fiber using an electric field-controlled fiber-to-fiber offset coupling. This innovative approach enables dynamic and controllable manipulation of modes by inducing deflection in the coated fiber through the electric field. This technology opens up possibilities for applications in sensing, communications, and beyond. By adjusting the experimental parameters, the sensitivity of the system can be tuned to meet specific requirements. This new automated mode-switching approach will be well-suited for field deployment in varying operational environments and should be useful in higher order applications in photonics and fiber circuits.

IV. REFERENCES

[1] A. K. Memon, and K. X. Chen, Opto-Electronics Review, 29 (2021).
[2] Isha Sharma, Partha Roy Chaudhuri, Optical Fiber Technology, 62 (2021) 102472